Journal of Biomedical Optics 9(6), 1152–1160 (November/December 2004)

Near-infrared imaging of the human breast: complementing hemoglobin concentration maps with oxygenation images

Erica Heffer
Vivian Pera*
Tufts University
Department of Biomedical Engineering
Bioengineering Center
4 Colby Street
Medford, Massachusetts 02155

Oliver Schütz
Horst Siebold
Siemens AG, Medical Solutions
Erlangen, Germany

Sergio Fantini
Tufts University
Department of Biomedical Engineering
Bioengineering Center
4 Colby Street
Medford, Massachusetts 02155
E-mail: sergio.fantini@tufts.edu

Abstract. We have previously reported a comparison between edge-corrected near-infrared optical mammograms and those that have undergone a further image-processing step based on a spatial second derivative. In this work, we go a step further by combining the second-derivative images from four wavelengths (690, 750, 788, and 856 nm) to obtain oxygenation-index images. While the spatial second derivative improves contrast and allows for visibility of fine structures in the images, thereby improving the sensitivity to tumor detection, additional information is needed to avoid false-positive results. The oxygenation-index images are introduced to address this issue. Oxygenation information may help discriminate benign from malignant breast lesions, thereby effectively complementing single-wavelength optical mammograms that display optically dense regions within the breast with high sensitivity. [DOI: 10.1117/1.1805552]

Keywords: optical mammography; breast cancer; photon migration; hemoglobin; near-infrared spectroscopy.

Paper 03044 received Apr. 14, 2003; revised manuscript received Nov. 14, 2003; accepted for publication Nov. 24, 2003. This paper is a revision of a paper presented at the SPIE conference on Optical Tomography and Spectroscopy of Tissue V, Jan. 2003, San Jose, California. The paper presented there appears (unrefereed) in SPIE Proceedings Vol. 4955.

1 Introduction

Near-infrared imaging has been investigated as a promising method for biological imaging (particularly mammography) for the past several years. This is because light in the 700- to 900-nm wavelength range can penetrate through several centimeters of tissue and is highly sensitive to the hemoglobin concentration and oxygenation in tissue. In optical mammography, the absorption of hemoglobin is the main source of intrinsic optical contrast as a result of hemodynamic changes (angiogenesis, changes in blood flow, and oxygenation) at tumor sites.[1] In fact, it has been reported that tumors have hemoglobin concentrations that can be up to 2 to 4 times higher than surrounding healthy tissue,[2–5] thus potentially featuring a high intrinsic optical contrast.

It is this optical contrast that poses the basis for the optical detection of breast cancer. Several groups have been working on finding the actual absorption and scattering coefficients throughout the breast, with the idea that the absorption coefficients should be higher in the cancer location due to the local increase in hemoglobin concentration. This task requires solution of the inverse problem,[6–8] which is complicated by the fact that near-infrared light is highly scattered in biological tissue and photon paths cannot be determined easily.

Another approach to enhancing the intrinsic contrast consists of injecting optical contrast agents such as indocyanine green into the bloodstream.[9] In this case, in the absence of extravasation, areas with higher concentrations of blood vessels will be observed with higher optical contrast. Although optical contrast is a key requirement for tumor detection, it is not necessarily enough to make a final determination as to the exact nature of the high-contrast region. Lesions that are not cancer, such as hematomas, mastopathies, or fibroadenomas, can cause high optical contrast as well. It is for this reason that many groups are attempting to enhance observed increases in local blood volume afforded through optical contrast, with more functional information such as oxygen saturation[2–4,6,7,10] or dynamic behaviors[11] to discriminate these types of lesions once the location is known.

We present a method to complement single-wavelength, contrast-enhanced images with multiwavelength, oxygenation index images. The starting points are the amplitude and phase images collected with a frequency-domain optical mammography prototype developed by Siemens Medical Solutions, Erlangen, Germany. The image is contrast enhanced using a two-step algorithm. The first step combines amplitude and phase data to account for photon losses and variable tissue thickness at the edge of the breast, resulting in so-called N images.[12] The second step consists of an algorithm based on a spatial second derivative, thus leading to N'' images.[13] The N'' images allow for high-contrast visualization of regions of increased optical attenuation within the breast. Although such

Address all correspondence to Sergio Fantini, Tufts Univ., Dept. of Biomedical Engineering, 4 Colby St., Medford, MA 02155. Fax: 617-627-3231; E-mail: sergio.fantini@eecs.tufts.edu
*Current affiliation: MIT Lincoln Laboratory, 244 Wood Street, Lexington, MA 02420-9108.

1083-3668/2004/$15.00 © 2004 SPIE

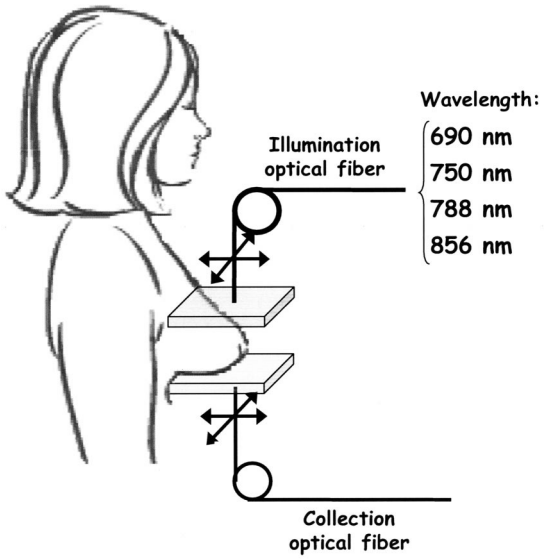

Fig. 1 Patient's arrangement in the optical breast examination. The breast is slightly compressed between the two glass plates. Source and detection fibers are located collinearly on the top and bottom of the breast and are scanned in tandem in a raster pattern. In the configuration shown, cranio-caudal views are obtained, and oblique views are obtained by rotating the glass plates by 45 deg.

enhanced contrast allows for the visualization of areas characterized by a higher optical density (as is usually the case for cancer, blood vessels, and a large class of benign lesions), they do not always enable discrimination between these different breast inhomogeneities. We believe that the key to discerning cancer from benign lesions and normal breast inhomogeneities lies in functional information such as the oxygenation level of the region. In fact, *in-vivo* oxygen tension measurements have indicated that cancer is typically associated with a lower oxygenation than healthy tissue and benign lesions.[14,15] Furthermore, near-infrared breast studies have already indicated the potential discrimination of benign and malignant lesions on the basis of their oxygenation.[7,10,16–18] While it is yet to be established if the oxygenation level of a breast lesion can be used to reliably discriminate cancer from benign lesions and normal tissue structures, oxygenation measurements provide important metabolic information. Such information may prove to be valuable in diagnostic imaging of the breast and to enhance the performance of optical mammography.

In our method, functional information is provided in the form of an oxygenation index. It is derived from the analysis of N'' images at four wavelengths, and although these are not absolute measurements of the tissue oxygenation, they still allow for the comparison of oxygenation levels of different areas in breast images.

2 Methods

The raw optical data were collected using a frequency-domain optical mammography prototype that was developed by Siemens Medical Solutions, Erlangen, Germany, the details of which have been described elsewhere.[19,20] Figure 1 shows the patient setup. The breast is slightly compressed between two glass plates where source and detection fibers are located collinearly on either side of the breast. Cranio-caudal views of the breast are obtained in the configuration shown in Fig. 1, while oblique views are obtained by rotating the glass plates by 45 deg. Intensity-modulated (70-MHz) lasers emitting at four wavelengths (690, 750, 788, and 856 nm) are coupled to the source fiber. The fibers are then scanned in tandem in a raster pattern over the entire area of the breast.

2.1 *Single-Wavelength Structural Images*

The raw-data images show low contrast for breast inhomogeneities because of the large dynamic range caused by the relatively large difference between the tissue thickness in the central area and at the edge of the breast. To correct for the effects of breast thickness variability across the image, we introduced an edge-correction algorithm resulting in so-called N images, which has been presented in a previous publication.[12] In short, edge corrected N values are calculated at each pixel using a reference point at the center of the breast and combining the phase and amplitude information from this point with that of every other point in the breast. The N value is related to the optical attenuation of the tissue, so the higher the N value, the higher the optical attenuation.

To further enhance the contrast in these images, we have applied an algorithm that computes the spatial second derivative of the N images (N'' images). This algorithm is described in detail elsewhere.[13] The steps involved in this algorithm include: convolution of the data with a smoothing function to minimize the effects of noise; taking the spatial second derivative in four directions (horizontal, vertical, and two diagonals); taking the minimum of the four directional results to enhance the display of directional structures; displaying pixels with a negative second-derivative value using a grayscale palette; and displaying pixels with a positive second-derivative in white.

2.2 *Multiple-Wavelength Functional Images*

Information from the second-derivative images at four wavelengths is used to calculate what we call oxygenation index images. Each oxygenation index image is obtained by combining the information content of the corresponding N'' images at all four wavelengths (690, 750, 788, and 856 nm).

We have chosen to use N'' in the calculation of the oxygenation index because it maintains an approximate proportionality to the absorption perturbation $\Delta\mu_a$ over a relatively wide range of values of $\Delta\mu_a$. First-order perturbation theory, which describes relatively small perturbations, predicts that the negative intensity perturbation $-(\Delta I/I_0)$ associated with an absorbing inhomogeneity is proportional to $\Delta\mu_a$ (here, I_0 and ΔI are the edge-effect corrected background intensity and intensity change associated with the tumor, respectively). From the definition of N, it follows that $I=I_0/N$ and $-(\Delta I/I_0)=-(I-I_0)/I_0=1-1/N$, which in turn is approximately equal to $N-1$ in the first-order perturbation limit of $N\approx 1$. In addition to $1-1/N_{\max}$, we have also calculated $N_{\max}-1$ and $|N''|_{\max}$ (where the subscript "max" refers to the location of the maximum intensity perturbation) according to first-order perturbation theory for comparison. The equations for $1-1/N_{\max}$, $N_{\max}-1$, and $|N''|_{\max}$ using first-order pertur-

bation theory, for an absorbing perturbation that is equidistant from the source and detector, are the following:

$$-\left.\frac{\Delta I}{I_0}\right|_{\max} = 1 - \frac{1}{N_{\max}} = \frac{3V\mu'_{s0}\Delta\mu_a}{\pi r}, \tag{1}$$

$$N_{\max} - 1 = \frac{1}{1 - \left(\frac{3V\mu'_{s0}\Delta\mu_a}{\pi r}\right)} - 1, \tag{2}$$

$$|N''|_{\max} = \frac{4\left[\frac{(3\mu_{a0}\mu'_{s0})^{1/2}}{r} + \frac{2}{r^2}\right]\frac{\Delta\mu_a V 3\mu'_{s0}}{\pi r}}{\left(1 - \frac{V3\mu'_{s0}\Delta\mu_a}{\pi r}\right)^2}, \tag{3}$$

where μ_{a0} (μ'_{s0}) is the background absorption (reduced scattering) coefficient, $\Delta\mu_a$ is the difference between the absorption coefficient of the inclusion and of the background, r is the source-detector separation, and V is the volume of the inclusion. To consider a more realistic case, we have calculated $1-1/N_{\max}$, $N_{\max}-1$, and $|N''|_{\max}$ for a relatively large sphere (2 cm in diameter) and for values of $\Delta\mu_a$ up to 0.5 cm^{-1} (which are beyond the limits of validity of first-order perturbation) using publicly available software that computes the exact solution of the diffusion equation for a sphere embedded in an infinite medium.[21] In our calculations, the source-detector separation r was 6 cm, the sphere was equidistant from source and detector, and the background reduced scattering (μ'_{s0}) and absorption coefficients (μ_{a0}) were 8.0 and .04 cm^{-1}, respectively. Figure 2 compares the dependence of $1-1/N_{\max}$ [Fig. 2(a)], $N_{\max}-1$ [Fig. 2(b)], and $|N''|_{\max}$ [Fig. 2(c)] on $\Delta\mu_a$ according to first-order perturbation theory (dashed lines) and the exact solution to the diffusion equation for a 2-cm-diam sphere (thick solid lines). Figure 2(a) shows that $1-1/N_{\max}$ (which is proportional to $\Delta\mu_a$ in first-order perturbation theory) deviates from the linear dependence of first-order perturbation by more than 10% for $\Delta\mu_a > 0.04\,\text{cm}^{-1}$. The value of $N_{\max}-1$ [Fig. 2(b)] deviates from the linear trend in the limit $\Delta\mu_a \to 0$ by more than 10% at $\Delta\mu_a > 0.12\,\text{cm}^{-1}$. Figure 2(c) shows that $|N''|_{\max}$ does not deviate from a proportional dependence on $\Delta\mu_a$ by more than 8% over the whole range of $0 < \Delta\mu_a < 0.5\,\text{cm}^{-1}$ considered by us.

On the basis of the results of Figs. 2(a), 2(b), and 2(c), we have opted to use $|N''|_{\max}$ for the oxygenation index calculations, as it is closer to being directly proportional to $\Delta\mu_a$ than either $N_{\max}-1$ or $1-1/N_{\max}$. In fact, to obtain the oxygen saturation of hemoglobin, it is sufficient to measure the absorption coefficient to within a multiplicative factor. Figure 3 gives an indication as to why $N_{\max}-1$ and $|N''|_{\max}$ behave differently. Here, the calculated $N_{\max}-1$ values (using diffusion theory for a sphere) for the range of $\Delta\mu_a$ from 0.05 to 0.50 cm^{-1} are normalized and plotted with respect to the source-detector scanning coordinate across the sphere. As $\Delta\mu_a$ is increased, there is an increase in $|N''|_{\max}$ (i.e., a narrowing of the peak as $N_{\max}-1$ increases). This accounts for the difference in behavior between $N_{\max}-1$ and $|N''|_{\max}$ versus $\Delta\mu_a$.

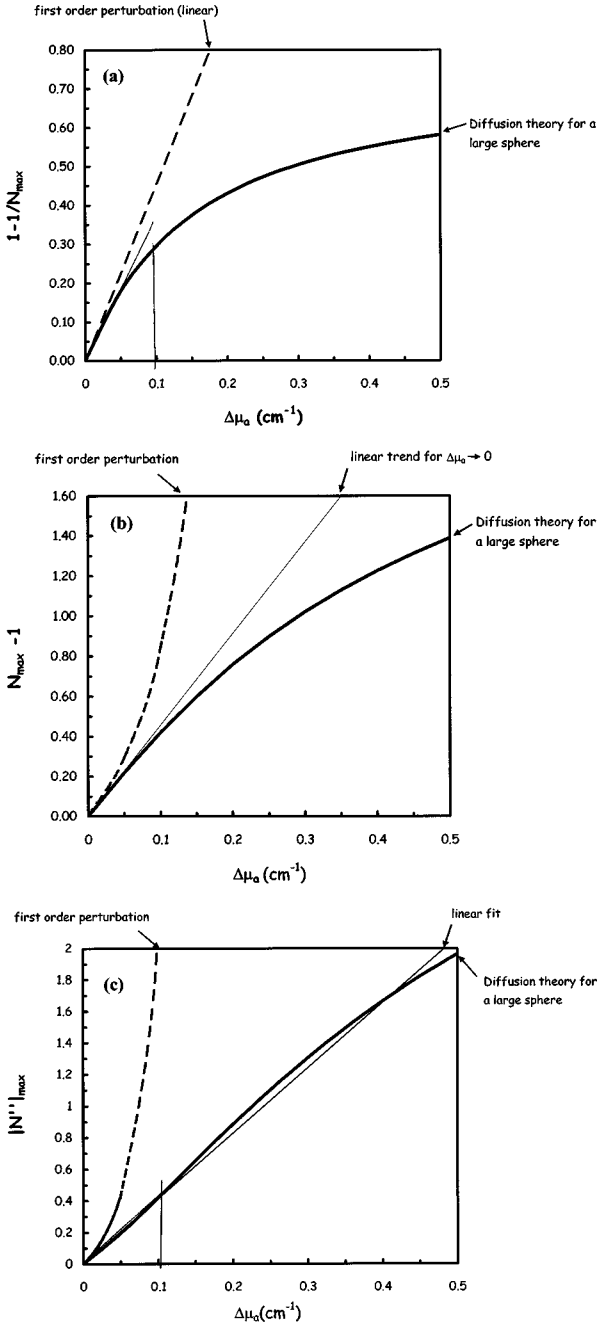

Fig. 2 Comparison of the dependence of (a) $1-1/N_{\max}$, (b) $N_{\max}-1$, and (c) $|N''|_{\max}$ on $\Delta\mu_a$ for a 2-cm-diam spherical object embedded in a turbid medium according to first-order perturbation theory (dashed lines) and the exact solution to the diffusion equation (thick lines).

The size and absorption contrast featured by breast lesions is often beyond the range of applicability of first-order perturbation theory. Since the proportionality between $|N''|_{\max}$ and $\Delta\mu_a$ is only approximately satisfied and may be affected by the size, shape, or depth of the tumor, we introduce a star in $\Delta[\text{HbO}_2]^*$ and $\Delta[\text{Hb}]^*$ to indicate pseudovalues of the changes in the concentrations of oxyhemoglobin and deoxyhemoglobin, respectively, as calculated using $|N''|_{\max}$. These pseudovalues of oxy- and deoxyhemoglobin are calculated in the following equations:

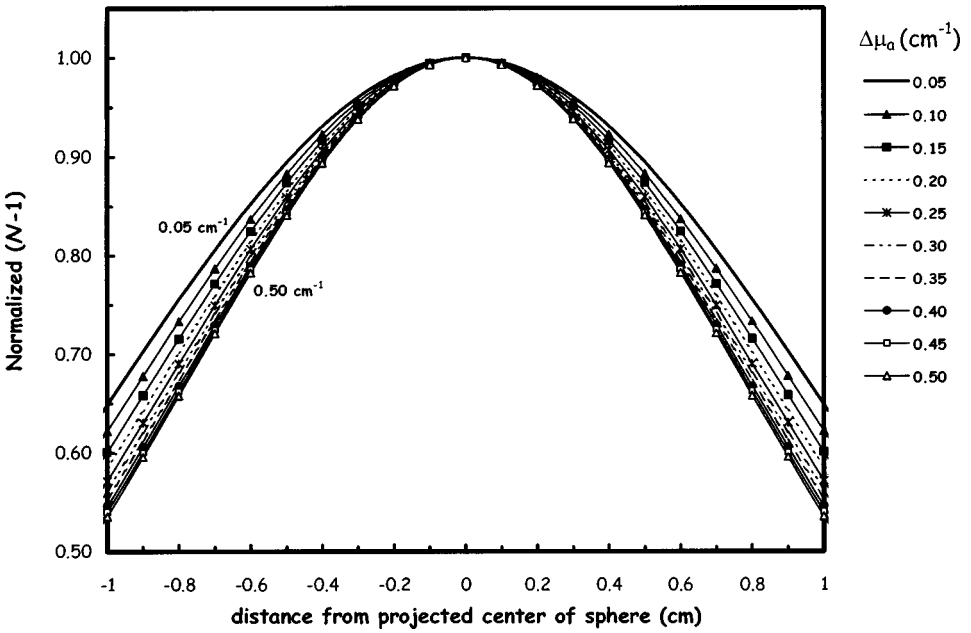

Fig. 3 Plots of normalized values of $N-1$ over a distance of −1 to +1 cm from the projected center of the sphere showing the narrowing of the peak as $\Delta\mu_a$ increases.

$$\Delta[\mathrm{HbO_2}]^* = \frac{[\Sigma_i N''(\lambda_i)\epsilon_{\mathrm{HbO_2}}(\lambda_i)][\Sigma_i \epsilon^2_{\mathrm{Hb}}(\lambda_i)] - [\Sigma_i N''(\lambda_i)\epsilon_{\mathrm{Hb}}(\lambda_i)][\Sigma_i \epsilon_{\mathrm{HbO_2}}(\lambda_i)\epsilon_{\mathrm{Hb}}(\lambda_i)]}{[\Sigma_i \epsilon^2_{\mathrm{HbO_2}}(\lambda_i)][\Sigma_i \epsilon^2_{\mathrm{Hb}}(\lambda_i)] - [\Sigma_i \epsilon_{\mathrm{HbO_2}}(\lambda_i)\epsilon_{\mathrm{Hb}}(\lambda_i)]^2}, \tag{4}$$

$$\Delta[\mathrm{Hb}]^* = \frac{[\Sigma_i N''(\lambda_i)\epsilon_{\mathrm{Hb}}(\lambda_i)][\Sigma_i \epsilon^2_{\mathrm{HbO_2}}(\lambda_i)] - [\Sigma_i N''(\lambda_i)\epsilon_{\mathrm{HbO_2}}(\lambda_i)][\Sigma_i \epsilon_{\mathrm{HbO_2}}(\lambda_i)\epsilon_{\mathrm{Hb}}(\lambda_i)]}{[\Sigma_i \epsilon^2_{\mathrm{HbO_2}}(\lambda_i)][\Sigma_i \epsilon^2_{\mathrm{Hb}}(\lambda_i)] - [\Sigma_i \epsilon_{\mathrm{HbO_2}}(\lambda_i)\epsilon_{\mathrm{Hb}}(\lambda_i)]^2}. \tag{5}$$

Here, i is the wavelength index, and $\epsilon_{\mathrm{HbO_2}}$ and ϵ_{Hb} are the molar extinction coefficients of oxyhemoglobin and deoxyhemoglobin, respectively.[22] The oxygenation index is calculated by combining these pseudovalues of the oxy- and deoxyhemoglobin in the following equation:

$$\text{oxygenation index} = \frac{\Delta[\mathrm{HbO_2}]^*}{\Delta[\mathrm{HbO_2}]^* + \Delta[\mathrm{Hb}]^*}. \tag{6}$$

If we were to replace $N''(\lambda_i)$ with the actual $\Delta\mu_a(\lambda_i)$ in Eqs. (4) and (5), we would calculate the actual oxygen saturation associated with $\Delta\mu_a$ in Eq. (6).[23] The oxygenation index is only calculated for pixels that have a negative second derivative at all four wavelengths, and is displayed in a rainbow color scale. Out of the total number of pixels for which the oxygenation index was calculated, 2.5% with the highest and lowest values were eliminated as outliers.

3 Results

Here we present the results for four human cases where we show N images, N'' images, and oxygenation index images. Although N images and N'' images have been compared previously,[13] we present them here to illustrate their complementary information content with respect to the multiwavelength oxygenation index images. The first three cases (patient numbers 311, 233, and 258) show images of cancer-bearing breasts. The fourth case (patient number 195) shows a benign fibroadenoma in the right breast. For each of these cases, we know the location, size, and type of breast lesion from x-ray mammography and pathology reports.

3.1 *Optical Images*

3.1.1 *Case 1: Patient number 311, 2.5-cm invasive ductal carcinoma, left breast*

Figure 4 refers to an 82 year old patient with a 2.5-cm invasive ductal carcinoma in the left breast. In the N image of Fig. 4(a), there is a dark region at $9.5\,\mathrm{cm} < x < 11.5\,\mathrm{cm}$ and $6.0\,\mathrm{cm} < y < 8.0\,\mathrm{cm}$ that corresponds to the cancer location. However, there are also other areas of increased contrast in this image that do not correspond to the cancer location. At $7.0\,\mathrm{cm} < x < 10.0\,\mathrm{cm}$ and $2.0\,\mathrm{cm} < y < 4.0\,\mathrm{cm}$, there is an area of increased attenuation that does not correspond to cancer. The morphology indicates that this is a grouping of blood vessels. Another area of high optical contrast is located at $14.0\,\mathrm{cm} < x < 16.0\,\mathrm{cm}$ and $6.0\,\mathrm{cm} < y < 10.0\,\mathrm{cm}$. Again, this does not correspond to a region containing cancer, and its elongated shape is consistent with a blood vessel.

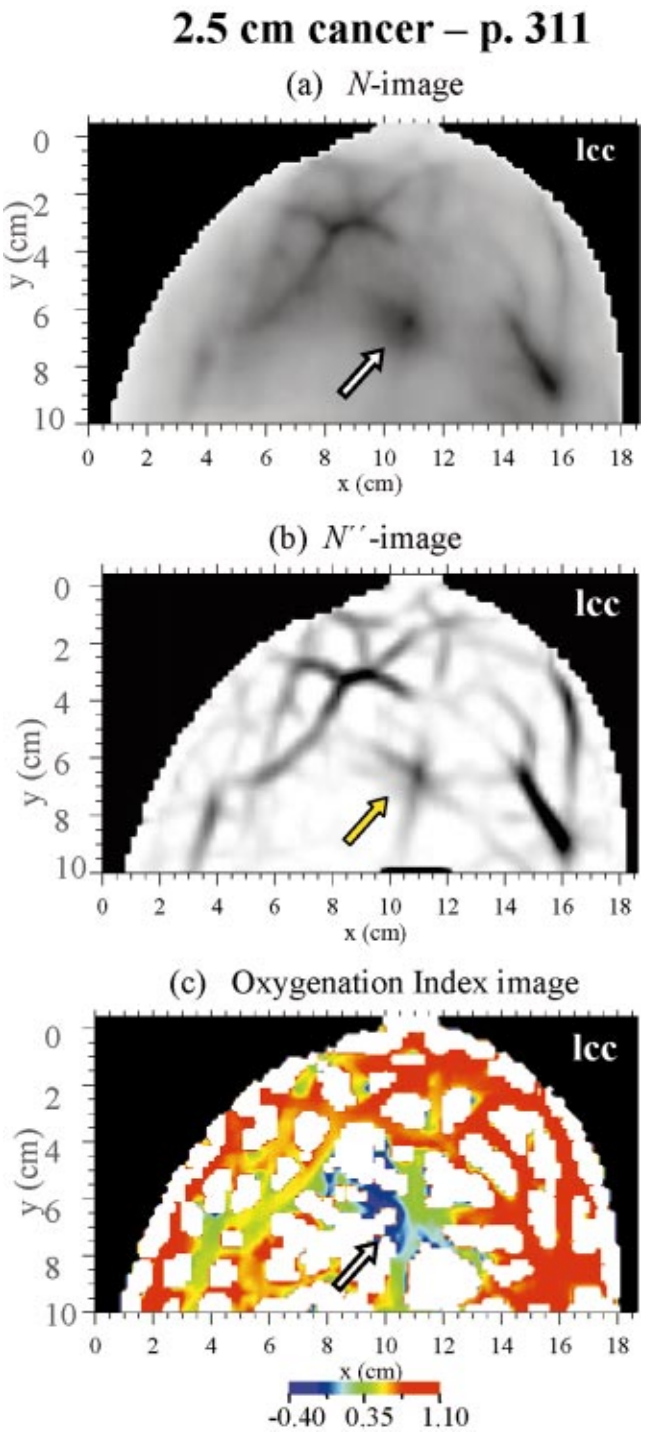

Fig. 4 Patient number 311, 82 years old, 2.5-cm-diam invasive ductal carcinoma in the left breast. The left cranio-caudal (lcc) view is shown. The arrows in each panel indicate the location of the cancer. (a) *N*-image: combination of amplitude and phase data to correct for edge effects. The areas of increased contrast are due mainly to a local increase in total hemoglobin. (b) *N*″-image: regions where the spatial second derivative is positive are displayed in white, and regions where the spatial second derivative is negative are displayed in gray-scale. (c) oxygenation index image: the oxygenation index is calculated for pixels where the *N*″ value is negative at all four wavelengths (690, 750, 788, and 856 nm). It is then displayed on a rainbow color scale where blue indicates low oxygenation and red indicates high oxygenation.

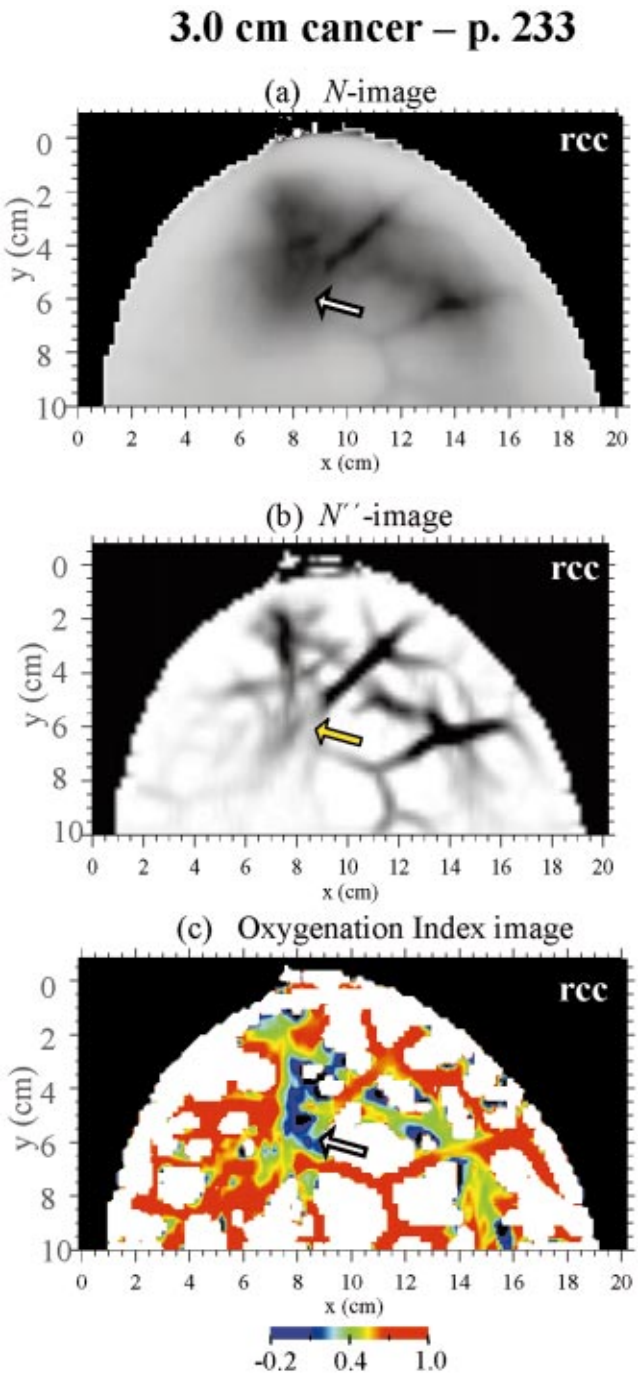

Fig. 5 Patient number 233, 67 years old, 3.0-cm-diam invasive ductal carcinoma in the right breast, cranio-caudal (rcc) view. The arrow indicates the location of the cancer. (a) *N* image, (b) *N*″ image, and (c) oxygenation index image for patient number 233.

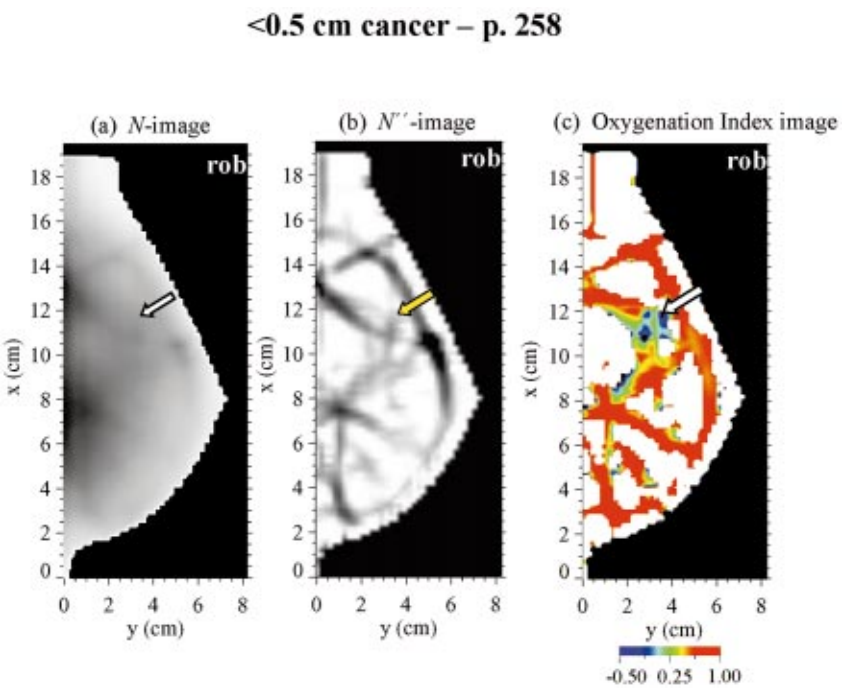

Fig. 6 Patient number 258, 47 years old, <0.5-cm-diam invasive ductal carcinoma in the right breast, oblique (rob) view. The arrow indicates the location of the cancer. (a) *N* image, (b) *N*″ image, and (c) oxygenation index image for patient number 258.

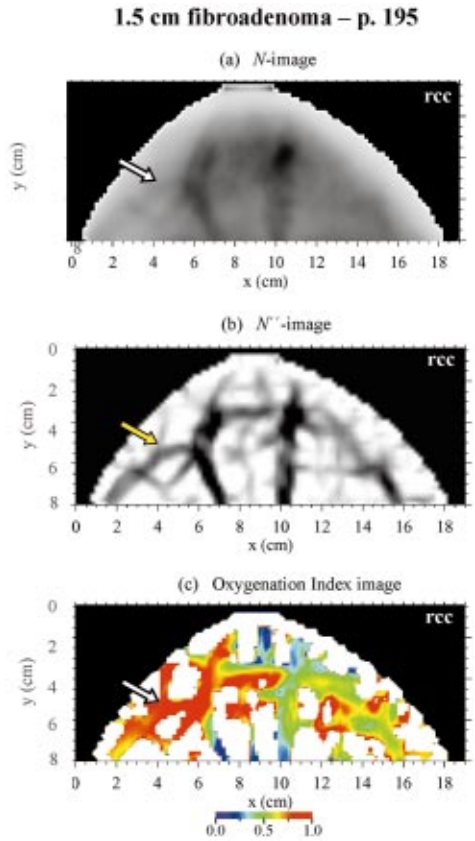

Fig. 7 Patient number 195, 51 years old, 2.0- ×1.5-cm-diam fibroadenoma in the right breast, cranio-caudal (rcc) view. The arrow indicates the location of the fibroadenoma. (a) *N* image, (b) *N*″ image, and (c) oxygenation index image for patient number 195.

In the N'' image shown in Fig. 4(b), the features seen in the N image appear with finer detail. For example, features that appeared as blurred regions of increased contrast now distinctly show the morphology of blood vessels. In agreement with what appears in the N image, there is a dark area corresponding to the cancer location; however, morphology indicative of vasculature is apparent in the N'' image. Other regions that appear with high contrast in this image ($7.0\,\text{cm}<x<10.0\,\text{cm}$, $2.0\,\text{cm}<y<4.0\,\text{cm}$, and $14.0\,\text{cm}<x<16.0\,\text{cm}$, $6.0\,\text{cm}<y<10.0\,\text{cm}$ just as in the N image) show their vascular nature more definitively as well. From these images alone it is not possible to discriminate the cancer from other areas of the breast that simply contain blood vessels. This leads us to the oxygenation index image shown in Fig. 4(c). The color representation in the oxygenation index images displays regions of lower oxygenation in blue and regions with higher oxygenation in red. Many of the regions that appear with high contrast in the N image and the N'' image correspond to relatively high values of oxygenation, whereas the region containing the cancer has reduced oxygenation.

3.1.2 *Case 2: Patient number 233, 3.0-cm invasive ductal carcinoma, right breast*

The results in Fig. 5 are from a 67 year old patient with a 3.0-cm invasive ductal carcinoma in the right breast. The N image shown in Fig. 5(a) shows a rather diffuse dark spot at $7.0\,\text{cm}<x<10.0\,\text{cm}$, $3.0\,\text{cm}<y<6.0\,\text{cm}$ that corresponds to the cancer location. There are several other regions in the N image of Fig. 5(a) that appear dark, but do not correspond to the cancer location.

There is a marked change in the visible features between the N image and the N'' image [Fig. 5(b)]. Namely, the region that contains the cancer appears with lower contrast in the N'' image than it does in the N image, while the other regions (clearly showing the morphology of blood vessels here) show a much higher contrast than previously. While it is difficult to detect the cancer from the N image and the N'' image alone, the cancer location can be discriminated in the oxygenation index image in Fig. 5(c), because it corresponds to a region of lower oxygenation.

3.1.3 *Case 3: Patient number 258, <0.5-cm cancer, right breast*

The images in Fig. 6 are from a 47 year old patient with a small cancer (<0.5 cm) in the right breast in the location indicated by the arrow. The cancer is not visible in the N image [Fig. 6(a)], in part because of a high contrast structure in another location ($7.0\,\text{cm}<x<9.0\,\text{cm}$, $0.0\,\text{cm}<y<2.0\,\text{cm}$) that expands the dynamic range of the N image. More information is afforded in the N image [Fig. 6(b)], where the region of high contrast appears to be due to a group of blood vessels. Furthermore, the N'' image shows additional blood vessels at other areas, such as $11.0\,\text{cm}<x<14.0\,\text{cm}$, $0.0\,\text{cm}<y<3.0\,\text{cm}$. The area containing the cancer appears in the N'' image with higher contrast than in the N image, but it is not an outstanding feature. In the oxygenation index image [Fig. 6(c)], however, the cancer appears with high contrast as it is characterized by the lowest relative oxygenation in the image.

3.1.4 *Case 4: Patient number 195, 2.0×1.5-cm fibroadenoma, right breast*

The images shown in Fig. 7 are from a 51 year old woman with a 2.0×1.5 cm fibroadenoma in the right breast. The location of the fibroadenoma is not evident in the N image [Fig. 7(a)], but there are other locations that appear with high contrast: $6.0\,\text{cm}<x<8.0\,\text{cm}$, $4.0\,\text{cm}<y<8.0\,\text{cm}$, and at $9.5\,\text{cm}<x<11.0\,\text{cm}$, $3.5\,\text{cm}<y<5.5\,\text{cm}$. With the finer detail afforded by the N'' image, the morphology of blood vessels is evident at these locations and they appear with much higher contrast. In addition, the application of the second-derivative algorithm has revealed a region of increased attenuation at $3.0\,\text{cm}<x<6.0\,\text{cm}$, $4.0\,\text{cm}<y<7.0\,\text{cm}$, which corresponds to the location of the fibroadenoma. The oxygenation index image of Fig. 7(c) shows that the region containing the fibroadenoma corresponds to a relatively high oxygenation index in the image.

3.2 *Histograms*

3.2.1 *Case 1: Patient number 311*

Figure 8(a) shows the histogram for the values of oxygenation index in the image of Fig. 4(c). The range of oxygenation index values is from −0.4 to 1.1. The negative values of the oxygenation index reflect the fact that these are pseudo-oxygen saturation values, as discussed in Sec. 2.2. One should consider the relative value of oxygenation index across the image, rather than their absolute values. Pixels that correspond to the cancer region are shown in black, and it can be seen in the histogram of Fig. 8(a) that the pixels from the cancer region fall below an oxygenation index of 0.4, which is in the lower 63% of the full range of values. Oxygenation index values in healthy tissue fall mostly above this range, which represents 81% of the pixels in the image of Fig. 4(c).

3.2.2 *Case 2: Patient number 233*

Figure 8(b) shows the histogram for the values in the oxygenation index image in Fig. 5(c). The full range of oxygenation index in this case is 0.4 to 1.3. The cancer pixels are displayed in black, and they fall in the lower range of oxygenation index values, below 0.6, which is in the lowest 52% of the full range of values. The oxygenation index values represented in the healthy tissue mainly fall above 0.6, with 70% of all oxygenation index values in the image residing in the oxygenation index range between 0.6 and 1.3.

3.2.3 *Case 3: Patient number 258*

Figure 8(c) shows the histogram for the values in the oxygenation index images in Fig. 6(c). The full range of oxygenation index values is from −0.4 to 1.0 in this case. Again, the pixels corresponding to the cancer are displayed in black. In this case they fall below an oxygenation index value of 0.5, which is in the lowest 57% of the full range of values, while 80% of the values in the image fall between oxygenation index values of 0.5 and 1.0.

3.2.4 *Case 4: Patient number 195*

Figure 8(d) corresponds to the values in the oxygenation index image shown in Fig. 7(c). Pixels in the fibroadenoma are

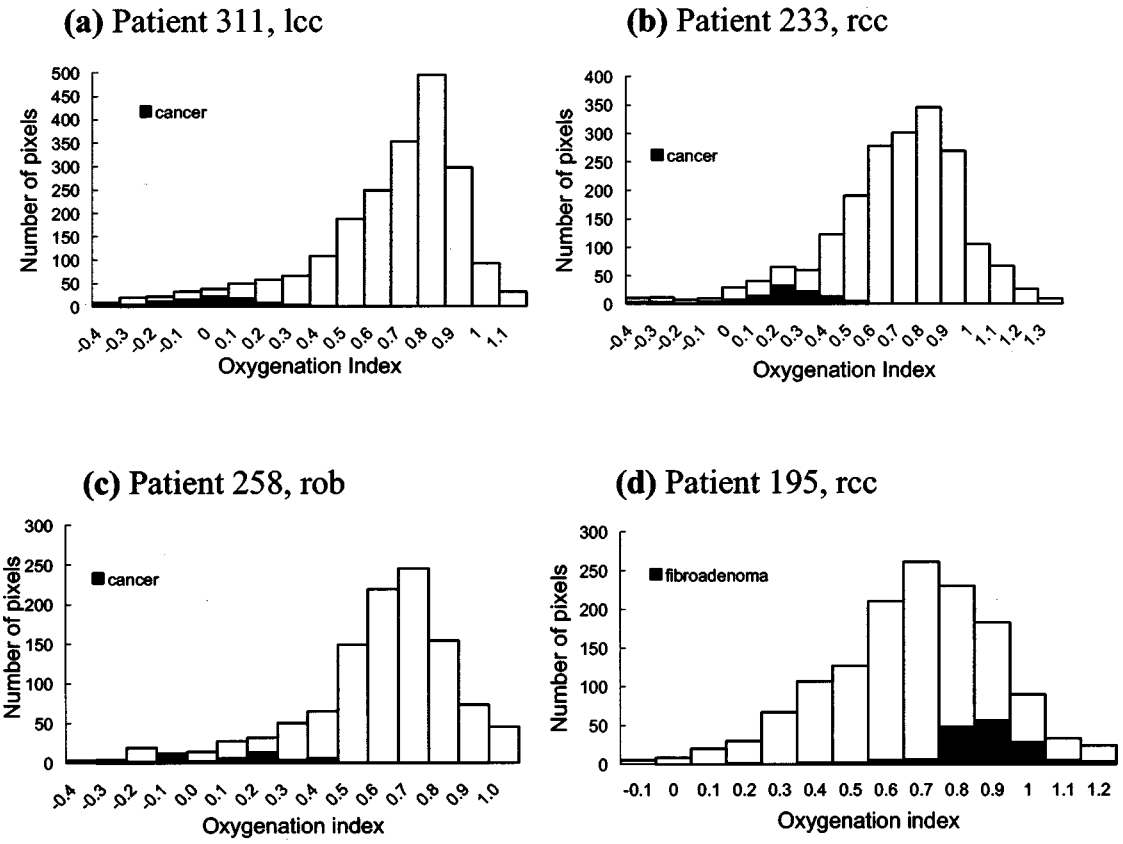

Fig. 8 Histograms corresponding to values in the oxygenation index images shown in Fig. 4. Pixels contained in the lesions under evaluation are displayed in black. (a) Patient 311, left cranio-caudal view (lcc), pixels in the cancer (black) fall below an oxygenation index value of 0.5 and are in the lower 63% of the full range of values. (b) Patient 233, right cranio-caudal view (rcc), pixels in the cancer (black) fall below an oxygenation index value of 0.7 and are in the lower 52% of the full range of values. (c) Patient 258, right oblique view (rob), pixels in the cancer (black) fall below an oxygenation index value of 0.5 and are in the lower 57% of the full range values. (d) Patient 195, right cranio-caudal view (rcc), pixels in the fibroadenoma (black) fall above an oxygenation index value of 0.7.

shown in black. The full range in Fig. 8(d) is −0.1 to 1.2, and the majority of the values in the fibroadenoma are above 0.7, i.e., in the highest 60% of the full range.

4 Discussion

The optical mammograms in Figs. 4 through 7 show how the information content of N images, N'' images, and oxygenation index images complements each other. N images best identify the regions with the highest optical contrast in the breast. The cancer of Fig. 5(a) belongs to a high-contrast structure and is therefore easily visible in the N image. In general, N images are useful to evaluate the level of absorption contrast of a given structure in the breast. However, if the cancer is not the dominant feature in the breast, like in Fig. 6(a), N images may not adequately display the cancer. This problem is addressed by the second-derivative images that display areas associated with local maxima in absorption. The contrast in the N'' images is not determined by the absorption contrast, as is the case in N images, but rather by the spatial curvature of the absorption peaks. As a result, relatively small structures such as blood vessels typically appear with high contrast in N'' images. Structures displayed in N images also appear in the N'' image, sometimes with a different contrast, like the cancer in Fig. 5(b). However, it is also possible to identify structures in the N'' images that are not readily visible in the N images, such as the cancer in Fig. 6(b). The price to pay for the increased sensitivity of N'' images is a reduced specificity for cancer detection. The oxygenation-index images, the focus of this work, are introduced to enhance the specificity by providing information on the local metabolic rate of oxygen at detected lesions. The potential of the oxygenation-index images to identify areas with higher oxygen metabolism is shown in Figs. 4(c), 5(c), and 6(c), where cancers are clearly displayed as areas of low oxygenation, while a benign lesion [the fibroadenoma of Fig. 7(c)] is associated with relatively high values of oxygenation.

The general feasibility of discriminating benign and malignant breast lesions on the basis of their oxygenation level (or, more exactly, the oxygen saturation of hemoglobin at the lesion location) is yet to be demonstrated. Despite the promising indications of oxygen tension studies and noninvasive optical studies, some results suggest that cancers may not always be associated with hypoxia. For example, Grosenick et al.[18] have reported a time-domain optical mammography study that showed a consistently higher hemoglobin concentration and lower (but sometimes comparable) blood oxygen saturation at cancerous lesions with respect to normal breast tissue. One of the difficulties of noninvasive optical oximetry of breast le-

sions involves the assessment of the local oxygenation of the lesion separately from the oxygenation of surrounding tissue. Some approaches, including the study by Grosenick et al.,[18] use a homogeneous model that combines the lesion and background oxygenation into an effective value.[3,4] In this work, we use the second derivative of N (N'') in an attempt to be sensitive to the absorption contrast of the lesion ($\Delta\mu_a$), at least to within a factor, independently of background absorption. This may lead to a meaningful comparison of the oxygenation levels of different areas within an image. However, the relative nature of the oxygenation index introduced here does not allow a comparison between the oxygenation values of lesions in different images. One of the ways this can be addressed is by obtaining more accurate oxygenation saturation values using a technique that is insensitive to the size, depth, and shape of the lesion.[24] In doing this, a more accurate assessment of the oxygenation values could be attributed to different types of lesions such as mastopathies, fibroadenomas, and cancers, thus leading to a more meaningful comparison of oxygenation values measured in different images and across patients.

5 Conclusions

We present a novel approach to combine multiple single-wavelength images to obtain multiwavelength functional information. The information in the single-wavelength images is now complemented by a multiwavelength image that provides indications as to the oxygenation throughout the breast. We show four cases where the use of these oxygenation images can help to discriminate benign and malignant lesions on the basis of their oxygenation level relative to the rest of the images. With the addition of a method to obtain the absolute oxygenation of breast lesions, the combination of high-contrast, second-derivative images and oxygenation images shows potential to improve the performance of diagnostic optical mammography in terms of sensitivity and specificity.

Acknowledgments

We thank Sylvia Heywang-Köbrunner, Linda Götz, and Anke Heinig for providing the clinical data for the patients reported in this study. This research is sponsored by the National Science Foundation, award BES-0093840, and by the National Institute of Health, Grant CA095885.

References

1. P. Vaupel, F. Kallinowski, and P. Okunieff, ''Blood flow, oxygen and nutrient supply, and metabolic microenvironment of human tumors: a review,'' *Cancer Res.* **49**, 6449–6465 (1989).
2. S. Fantini, S. A. Walker, M. A. Franceschini, M. Kaschke, P. M. Schlag, and K. T. Moesta, ''Assessment of the size, position, and optical properties of breast tumors *in vivo* by non-invasive optical methods,'' *Appl. Opt.* **37**, 1982–1989 (1998).
3. J. B. Fishkin, O. Coquoz, E. A. Anderson, M. Brenner, and B. J. Tromberg, ''Frequency-domain photon migration measurements of normal and malignant tissue optical properties in a human subject,'' *Appl. Opt.* **36**, 10–20 (1997).
4. B. J. Tromberg, O. Coquoz, J. B. Fishkin, T. Pham, E. R. Anderson, J. Butler, M. Cahn, J. D. Gross, V. Venugopalan, and D. Pham, ''Non-invasive measurements of breast tissue optical properties using frequency-domain photon migration,'' *Philos. Trans. Royal Soc. London, Series B-Biolog. Sci.* **352**, 661–668 (1997).
5. A. E. Profio and G. A. Navarro, ''Scientific basis of breast diaphanography,'' *Med. Phys.* **16**, 60–65 (1989).
6. H. Dehghani, B. W. Pogue, S. P. Poplack, and K. D. Paulsen, ''Multiwavelength three-dimensional near-infrared tomography of the breast: initial simulation, phantom, and clinical results,'' *Appl. Opt.* **42**, 135–145 (2003).
7. M. J. Holboke, B. J. Tromberg, X. Li, N. Shah, J. Fishkin, D. Kidney, J. Butler, B. Chance, and A. G. Yodh, ''Three-dimensional diffuse optical mammography with ultrasound localization in a human subject,'' *J. Biomed. Opt.* **5**, 237–247 (2000).
8. J. C. Hebden, H. Veenstra, H. Dehghani, E. M. C. Hillman, M. Schweiger, S. R. Arridge, and D. T. Delpy, ''Three-dimensional time-resolved optical tomography of a conical breast phantom,'' *Appl. Opt.* **40**, 3278–3287 (2001).
9. V. Ntziachristos, A. G. Yodh, M. Schnall, and B. Chance, ''Concurrent MRI and diffuse optical tomography of breast after indocyanine green enhancement,'' *Proc. Natl. Acad. Sci. U.S.A.* **97**, 2767–2722 (2000).
10. B. Chance, E. Anday, E. Conant, S. Nioka, S. Zhou, and H. Long, ''Rapid and sensitive optical imaging of tissue functional activity, and breast,'' *OSA Trends in Optics and Photonics Vol. 21, Advances in Optical Imaging and Photon Migration*, J. G. Fujimoto and M. S. Patterson, Eds., pp. 218–225, Optical Society of America, Washington, DC (1998).
11. R. L. Barbour, H. L. Graber, Y. Pei, S. Zhong, and C. H. Schmitz, ''Optical tomographic imaging of dynamic features of dense-scattering media,'' *J. Opt. Soc. Am. A* **18**, 3018–3036 (2001).
12. S. Fantini, M. A. Franceschini, G. Gaida, E. Gratton, H. Jess, W. W. Mantulin, K. T. Moesta, P. M. Schlag, and M. Kaschke, ''Frequency-domain optical mammography: edge-effect corrections,'' *Med. Phys.* **23**, 149–157 (1996).
13. V. E. Pera, E. L. Heffer, H. Siebold, O. Schütz, S. Heywang-Köbrunner, L. Götz, A. Heinig, and S. Fantini, ''Spatial second-derivative image processing: An application to optical mammography to enhance the detection of breast tumors,'' *J. Biomed. Opt.* **8**(3), 517–524 (2003).
14. P. Hohenberger, C. Flegner, W. Haensch, and P. M. Schlag, ''Tumor oxygenation correlates with molecular growth determinants in breast cancer,'' *Breast Cancer Res. Treat* **48**, 97–106 (1998).
15. P. Vaupel, K. Schlenger, C. Knoop, and M. Hockel, ''Oxygenation of human tumors: evaluation of tissue oxygen distribution in breast cancer by computerized O_2 tension measurements,'' *Cancer Res.* **51**, 3316–3322 (1991).
16. B. J. Tromberg, N. Shah, R. Lanning, A. Cerussi, J. Espinoza, T. Pham, L. Svaasand, and J. Butler, ''Non-invasive *in vivo* characterization of breast tumors using photon migration spectroscopy,'' *Neoplasia* **2**, 26–40 (2000).
17. T. O. Mcbride, B. W. Pogue, E. D. Gerety, S. B. Poplack, U. L. Österberg, and K. D. Paulsen, ''Spectroscopic diffuse optical tomography for the quantitative assessment of hemoglobin concentration and oxygen saturation in breast tissue,'' *Appl. Opt.* **38**, 5480–5490 (1999).
18. D. Grosenick, K. T. Moesta, H. Wabnitz, J. Mucke, C. Stroszczynski, R. Macdonald, P. M. Schlag, and H. Rinneberg, ''Time-domain optical mammography: initial clinical results on detection and characterization of breast tumors,'' *Appl. Opt.* **42**, 3170–3186 (2003).
19. L. Götz, S. H. Heywang-Köbrunner, O. Schütz, and H. Siebold, ''Optische mammographie an präoperativen patientinnen,'' *Aktuelle Radiol.* **8**, 31–33 (1998).
20. S. Fantini, E. L. Heffer, M. A. Franceschini, L. Götz, A. Heinig, S. Heywang-Köbrunner, Oliver Schütz, and Horst Siebold, ''Optical mammography with intensity-modulated light,'' *Proc. OSA*, pp. 111–117 (2000).
21. D. A. Boas, R. Gaudette, and T. Gaudette, PMI software, see http://www.nmr.harvard.edu/DOT/resources/toolbox.htm.
22. S. Prahl, ''Tabulated molar extinction coefficient for hemoglobin in water,'' see http://omlc.ogi.edu/spectra/hemoglobin/summary.html.
23. M. Cope, ''The application of near-infrared spectroscopy to non-invasive monitoring of cerebral oxygenation in the newborn infant,'' PhD Thesis, University College London (1991).
24. E. L. Heffer and S. Fantini, ''Quantitative oximetry of breast tumors: a near-infrared method that identifies two optimal wavelengths for each tumor,'' *Appl. Opt.* **41**, 3827–3839 (2002).